Project Insight: Direct and Inverse Dynamic Model

Alexandre Acerra Gil (Graduation student ISAE-SUPAERO/ENSICA)
Aurélio de Aguiar Rodrigues (Graduation student ISAE-SUPAERO)
Supervized by:
Daniel Alazard (ISAE-SUPAERO/DCAS) and Naomi Murdoch (ISAE-SUPAERO/DEOS)

Abstract

In order to obtain more reliable results of interior structure and processes of Mars, this paper describes the influence of the mechanical noise caused by wind arising from the atmosphere of Mars, acting on a lander. This noise will interfere the results of seismological experiments on the planet. Using modelling of dynamic vibrations in flexible appendages, it will be possible to predict the magnitude of forces in lander feet acting on Martian ground. By means of soil deformation modelling of the signal transmitted by the forces applied on the ground, measurements of the noise arriving at the equipment responsible to collect seismic data (SEIS seismometer) may also be provided. The results confirm that the interference caused by winds in seismic prospecting, for high frequency bands, respects allowed requirements. In addition, we changed some input parameters to study their influence on mechanical noise responses.

1 Introduction

The NASA Discovery Program mission InSight (Interior Exploration using Seismic Investigations, Geodesy and Heat Transport) [1, 2] was selected by NASA to understand features concerning the seismicity of Mars. Scheduled for launching in 2018, the mission is designed to give scientists a better understanding of the planet's evolution, investigating the interior structure and processes of Martian soil.

InSight is based on the proven Phoenix Mars spacecraft and a lander with a multi-body system. The payload is composed of a Seismic Experiment for Internal Structures (SEIS), a heatflux experiment (HP3), a geodesy experiment (RISE) and a magnetometer (IFG) [2].

SEIS consists of a 3-axes very-broadband (VBB) sensor working in 0.01 Hz - 1 Hz and a 3-axes short-period (SP) sensor working on frequencies higher than 10 Hz. The distance from the lander center to the SEIS center is 2.59 meters.

In this paper, we will analyse the effects of Martian winds on the solar panels (appendages) of the lander, producing vibrations. In turn, these vibrations in the solar panels will be responsible for creating resultant forces on the three footpads of the lander. Therefore, it would be useful to develop a method to analyse the resultants of external forces on the lander feet. To do so, we will consider the theory of linear dynamic modeling and Direct Integration Methods for Dynamic Response of Multiple-Degree-of-Freedom (MDOF) Systems [3, 4, 5], more precisely for connections of a flexible appendage (see [3]).

The external forces, which affect the solar panels and the lander body, will appear as resultant forces acting on the three footpads of the lander and then these resulting forces are passed to Martian soil, in the format of seismic noise. Consequently, we will able to develop a model to represent and calculate the stress applied at the lander feet. After entering Martian regolith properties, we aim to understand the influence of this seismic noise on processing the seismic signal registered on SEIS.

The next step is estimate a seismic noise transmitted to the SEIS due to the stress exerted on the Martian soil by the lander footpads. For this analysis, the theory of Boussinesq [6] is used to model the mechanical noise from the direct motion of the Martian soil. A theory for vertical displacements of the seismometer is applied to calculate an induced tilt noise [7].The result is a spectrum of the lander mechanical noise that reaches SEIS.

Afterwards, we changed the parameters of wind amplitude, soil stiffness and distance from the center of SEIS to the center of lander to recognize how each aspect affects the seismic mechanical noise at SEIS, giving a better perception about the production of seismic noise and how is possible to minimize it.

Our results may not be applicable for all cases, owing to key uncertain parameters in the model and other considerations assumed throughout this paper, such as:

(i) uncertainties in Martian wind measurements;

(ii) variations in density, direction and speed of Martian wind;

(iii) we did not take into account the wind interaction with the lander body (creation of vortexes, for example);

(iv) uncertainties as to the mass properties of the lander;

The majority of uncertainties lie in Martian atmospheric properties and wind data.

2 Wind Modeling

The first missions to Mars exploration, Phoenix Mars Lander, Viking 1 Lander and Viking 2 Lander, have provided measurements of wind speeds and directions at a height of 2 meters above the Martian surface. All these measurements were achieved by a mechanical anemometer and are available on the Planetary Data System, as discussed in more details in [7]. Moreover, at this reference other relevant theories are presented, such as: wind speed variation with vertical distance from Martian surface, dynamic pressure of wind, day/night wind speed variation and linear extrapolation for wind speed squared spectra at high frequencies. It will not be discussed in this paper details of the theories above referenced, though we desire to know the acting resultant forces on the lander.

To calculate the resultant forces on the lander center of pressure, we evaluated the lift and drag forces exerted on the lander. The acting forces sum of the lander is a single 3-D resultant force on the lander center of pressure, defined by lander aerodynamic properties. Force of lift F_l and force of drag F_d are given by:

$$F_l = PS_{lift}C_l \tag{1}$$

$$F_d = PS_{drag}C_d \tag{2}$$

where S_{lift} and S_{drag} are the lander surface areas exposed to the lift and drag forces. C_l and C_d are the lander lift and drag coefficients (see Table 1).

In this paper C_l and C_d were selected assuming the critical vertical angle of attack of the wind for the InSight lander, 15°, provided by wind-tunnel tests [7].

P is the dynamic pressure defined by:

$$P(z) = \frac{\rho}{2}\left[\frac{\ln(z/z_0)}{\ln(z_r/z_0)}\right]^2 U_x(z_r)^2 \tag{3}$$

Values and definition of z, z_0, ρ and z_r are defined in Table 1. $U_x(z_r)^2$ is a wind speed squared spectra calculated from wind speed data, delivered by Phoenix Mars Lander, Viking 1 Lander and Viking 2 Lander.

The construction of the wind amplitude spectral density (ASD) is basically divided in two parts: for f<15 mHz and for $f \geq 15$ mHz, based on the distribution of wind speed squared amplitudes, provided by Phoenix wind data [7].

However, the Martian wind spectrum is not the same over a Martian day due to atmospheric behaviours. Wherefore, in this paper we considered only an amplitude of the wind speed squared spectra of 125 $m^2s^{-2}Hz^{-1/2}$, for f<15 mHz. This value is relative to an estimation of amplitude, corresponding to 70% of the time, for wind speed spectra in the [1 - 15] mHz bandwidth. That estimation is based on probabilistic calculation of Phoenix and Viking wind data. In case of $f \geq 15$ mHz, $U_x(z_r)^2$ is determined by:

Table 1: Parameters used in wind calculation

Parameters	**Values**
Surface roughness, z_0	0.01 m
Reference height for wind calculations, z_r	1.61 m
Panels height, z	1.07 m
Martian air density (Day), ρ	0.0155 $kgm{-}3$
Surface area of lander exposed to the lift force, S_{lift}	7.53 m^2
Surface area of lander exposed to the drag force, S_{lift}	7.53 m^2
Lander lift coefficient, C_l	0.6
Lander drag coefficient, C_d	0.23
Cut-off frequency, f_{cut}	0.015 Hz

$$f \geq f_{cut} : U_x(z_r)^2 = B\left(\frac{f}{f_{cut}}\right)^{-\frac{5}{3}} \; m^2s^{-2}Hz^{-1/2} \tag{4}$$

where B is the amplitude 125 $m^2s^{-2}Hz^{-1/2}$. The linear model of day wind speed squared spectra is shown in Figure 1.

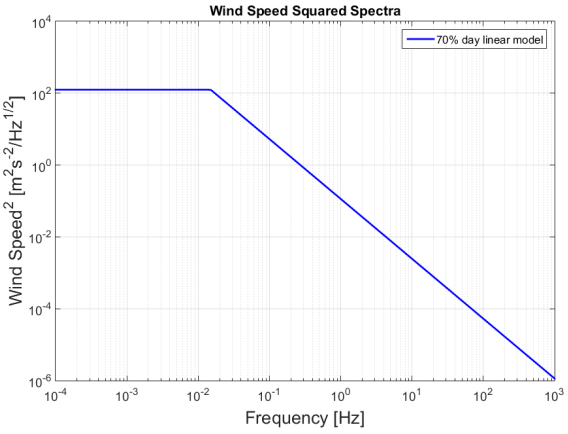

Figure 1: Wind speed squared spectra

For a horizontal wind direction, we assumed the most probable wind direction, expected to be 45° from the N-W and, as discussed before, we assumed a vertical direction is expected to be 15°.

3 Transmission of effort by flexible body model

The transmission of effort from the two panels to each lander footpad is studied by theory of direct dynamics model for case of a flexible appendage, based on Newton-Euler equations [3]. This model gives relation between inputs, composed of three components of external forces $\vec{F}_{ext}$, acting on any lander arbitrary point and three components of torques $\vec{T}_{ext,G}$, applied on the lander center of

mass G. The outputs are composed of three linear accelerations $\vec{a}_G$ and three angular accelerations $\vec{\omega}$. The theory about studies of Newton-Euler equations and transport of the dynamic model throughout the lander will not be discussed in details in this paper. See [3], [4] and [5].

3.1 Inverse dynamic model

In our model, we considered the case of rigid central body with 6 degrees-of-freedom (3 translations and 3 rotations), composed of the lander main body and their footpads, interconnected by two flexible appendages (solar panels). Moreover we assumed that the joints between the appendages and the main body are cantilevered [3].

A schematic illustration of the InSight lander is exposed in Figure 2, in order to provide a better understanding of the dynamic model, presented in this paper. Whereas an illustration of inputs and outputs of the inverse dynamic model is shown in Figure 3.

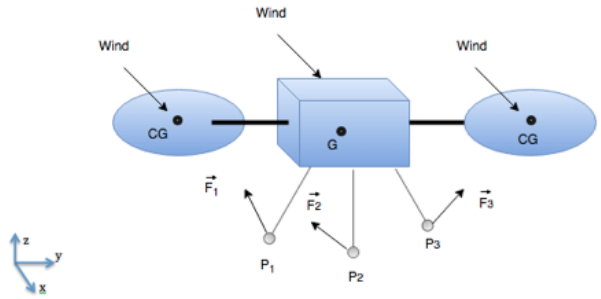

Figure 2: Schema of the InSight lander with a center of mass G.

Figure 3: Representation of the inverse dynamic model.

The inverse dynamic model $\left[D_G^{inSight}\right]^{-1}$ is expressed in Matlab/Simulink by a state-space representation of a linear system for p inputs, q outputs and n state variables, as written in the following form:

$$\begin{cases} \dot{x} = Ax + Bu \\ y = Cx + Du \end{cases}$$

where:

x *is the state vector*, $x(t) \in \mathbb{R}^n$;
y *is the output vector*, $y(t) \in \mathbb{R}^q$;
u *is the input (or control) vector*, $y(t) \in \mathbb{R}^p$;
A *is the state (or system) matrix*;
B *is the input matrix*;
C *is the output matrix*;
D *is the feedthrough (or feedforward) matrix*;

Equation 5 describes the modelling of the external forces $\vec{F}_{ext}$ and the external torques $\vec{T}_{ext,G}$ applied on the lander. They were split in four components: the first three components are the resultant force applied by the Martian soil, in each footpad and the last term is the aerodynamic forces applied on the lander center of pressure (CoP). As the components of force are applied out of the lander center of mass G, a kinematic model $[\tau_{P,G}]^T$ is used to make the translation of forces from a point P to the center of mass G.

$$\begin{bmatrix} \vec{F}_{ext} \\ \vec{T}_{ext,G} \end{bmatrix} = \sum_{i=1}^{3} [\tau_{P_i,G}]^T_{6x6} \begin{bmatrix} Fx_i \\ Fy_i \\ Fz_i \\ 0 \\ 0 \\ 0 \end{bmatrix} + [\tau_{CoP,G}]^T_{6x6} \begin{bmatrix} Fx_{aero} \\ Fy_{aero} \\ Fz_{aero} \\ 0 \\ 0 \\ 0 \end{bmatrix} \quad (5)$$

$$\begin{bmatrix} \vec{a}_G \\ \vec{\omega} \end{bmatrix} = \left[D_G^{inSight}\right]^{-1} \cdot \begin{bmatrix} \vec{F}_{ext} \\ \vec{T}_{ext,G} \end{bmatrix} \quad (6)$$

The six linear and angular accelerations on each lander footpad are calculated by Equation 6, which provided three non-zero components of linear acceleration and three null components of angular acceleration. These three null components are result of the external forces applied on the center of the mass.

An equilibrium equation [8] is used to create a three-dimensional soil-structure-interaction model $D_{P_i}^{Soil}$:

$$M\ddot{x} + C\dot{x} + Kx = F(t)$$

where M, C and K are generalized mass, damping and stiffness matrices, x is the displacement vector, where the dot denotes differentiation in respect of time and $F(t)$ is the unknown resultant force varying on time.

The acceleration, the velocity and the position vectors are, respectively, the linear acceleration $\vec{a}_G$ and their first and second integrals $\int \vec{a}_G$, $\iint \vec{a}_G$ applied on each footpad. Subsequently, the resultant force is looped in the system, as external forces of the lander feet Fx_i, Fy_i, Fz_i, using the kinematic model $[\tau_{P,G}]$ to produce the translation of

the components from the applied point on the footpad P and the lander center of gravity G. Figure 4 exemplifies the loop in the complete model:

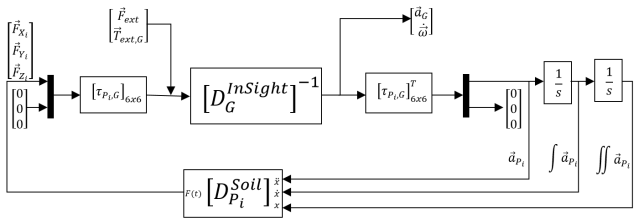

Figure 4: Complete Model.

In this case, only the stiffness parameters are considered in the soil model $D_{P_i}^{Soil}$, owing to the fact that stiffness is the only parameter available.

3.2 Regolith properties on Mars

Calculations of the regolith properties on Mars are made extrapolating of results found in laboratory, considering a reference pressure (p_{ref}) of 25 kPa and the upper 2 meters of regolith. The results obtained in the laboratory are shown in Table 2.

To calculate the pressure under each circular footpad of lander on Mars, Equation 7 is used (parameters values in Table 3).

$$p = \frac{mg_{Mars}}{\pi N_{feet} r_{feet}^2} \tag{7}$$

In the reference pressure, we assumed the condition of the minimum values from 3σ dispersion (see Table 3), extrapolating $p-$ and $s-$ wave velocities that act under each lander footpad. Thus,

$$V_{s,ref} = 150 - 3 \cdot 17 = 99 \ m/s$$

$$V_{p,ref} = 265 - 3 \cdot 18 = 216 \ m/s$$

Assuming the law based on laboratory measurements [7]. Equations 8 and 9 calculate $p-$ and $s-$ wave velocities from the regolith properties of Mars.

$$v_p = v_{p,ref} \left(\frac{p}{p_{ref}} \right)^{0.3} \tag{8}$$

$$v_s = v_{s,ref} \left(\frac{p}{p_{ref}} \right)^{0.3} \tag{9}$$

Afterwards using $p-$ and $s-$ wave velocities it is possible to calculate the Poisson's ratio (ν), Equation 10, and the Young's modulus of the Martial soil (E), Equation 11.

$$\nu = \frac{(v_p^2 - 2v_s^2)}{2(v_p^2 - v_s^2)} \tag{10}$$

Table 2: Parameters to calculating the regolith properties

Parameters	**Values**
Lander mass, m	365 kg
Martian surface gravity, g_{Mars}	3.71 ms^{-2}
Number of lander feet, N_{feet}	3
Radius of lander feet, r_{feet}	0.145 m

Table 3: Regolith properties predicted by laboratory [9]

Regolith Property	**Values**
Bulk Density, (ρ)	1665 +/− 38.3 kgm^{-3}
s-wave velocity, V_s	150 +/− 17 m/s
p-wave velocity, V_p	265 +/− 18 m/s

$$E = \rho v_s^2 \frac{(3v_p^2 - 4v_s^2)}{v_p^2 - v_s^2} \tag{11}$$

The ground stiffness K_s is calculated by Equation 12, using the factor E^*, Equation 13.

$$K_s = 2r_{feet} \cdot E^* \tag{12}$$

$$E^* = \frac{1}{\frac{1-\nu^2}{E} + \frac{1-\nu_f^2}{E_f}} \tag{13}$$

where ν_f and E_f are the Poisson's ratio and Young's modulus of the lander feet.

3.3 Final model

To adapt the model to the objectives of this project, a continuous-time linear state-space model $F(s)$ was created from the complete model, exposed in Figure 4. Considering the aerodynamic forces, as the inputs, and of the resultant forces on each footpad, as the outputs, it is possible to create the final system, represented in Figure 5:

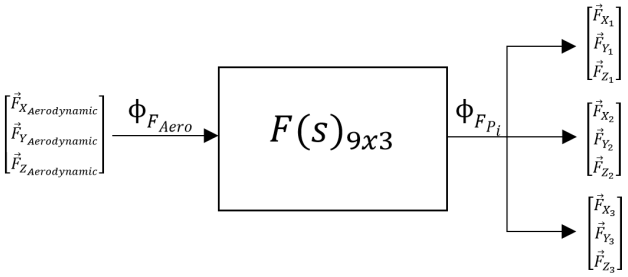

Figure 5: Final Model.

Equation 14 exposes the final modelling:

$$\phi_{F_{P_i}} = F(-s) \cdot \phi_{F_{aerodynamic}} \cdot F^T(s) \tag{14}$$

where the $\phi_{F_{P_i}}$ is the output, DSA forces on each footpad, $F(s)$ is the resultant state-space model and $\phi_{F_{aerodynamic}}$ is the input, DSA aerodynamic forces, calculated by the wind spectrum.

4 Ground deformation

In this section we discuss about the influence of the external forces on the lander feet that create seismic noise on the seismometer. We employed the Boussinesq point load solution [6] to calculate the deformation caused by those forces. We considered that the feet of lander and SEIS are on the surface of the regolith and the ground has an elastic deformations.

The fact of the feet of lander and SEIS are on the surface of the regolith simplifies the Green's tensor, as presented in [7]. Equation 15 is the Green's tensor representation for displacements (G_{ik}).

$$(G_{ik}) = \frac{1}{4\pi\mu}\begin{bmatrix} \frac{b}{r}+\frac{x^2}{r^3}-\frac{ax^2}{r^3} & \frac{xy}{r^3}-\frac{ayx}{r^3} & -\frac{ax}{r^2} \\ \frac{yx}{r^3}-\frac{ayx}{r^3} & \frac{b}{r}+\frac{y^2}{r^3}-\frac{ay^2}{r^3} & -\frac{ay}{r^2} \\ -\frac{ax}{r^2} & -\frac{ay}{r^2} & \frac{b}{r} \end{bmatrix} \quad (15)$$

where $\mu = \rho v_s^2$ is the shear modulus, $b = 2(1-\nu)$, r is the magnitude of the vector between an arbitrary point ($\mathbf{\Lambda} = \Lambda_1\mathbf{e_1} + \Lambda_2\mathbf{e_2} + \Lambda_3\mathbf{e_3}$) and a point where the force is applied ($\xi = \xi_1\mathbf{e_1} + \xi_2\mathbf{e_2} + \xi_3\mathbf{e_3}$), $x = \Lambda_1\xi_1$, $y = \Lambda_2\xi_2$ and $z = \Lambda_3\xi_3$.

It is useful to calculate the acceleration created by the vertical displacements of the seismometer that causes an inclination in the gravitational field. Considering small angle approximation, these accelerations may be calculated by:

$$A_{x_{tilt}} = g_{mars}\left[\frac{\frac{\Delta z_2+\Delta z_3}{2}-\Delta z_1}{x_1-x_2}\right] \quad (16)$$

$$A_{y_{tilt}} = g_{mars}\left[\frac{\Delta z_2-\Delta z_3}{y_3-y_2}\right] \quad (17)$$

where $A_{x_{tilt}}$ and $A_{y_{tilt}}$ are the acceleration due to the tilt in x- and y- axes; Δz_1, Δz_2 and Δz_3 are the displacement in z-axis of the three seismometer feet; x_1, x_2, y_2 and y_3 are coordinates of the x- and y- axes of the SEIS feet.

The component in z-axis of the tilt acceleration is negligible. Therefore, total noise in x- and y- axes are the sum of the accelerations from the ground direct motion and the tilt accelerations. In the z- axis acts only acceleration from the ground direct motion.

Figure 6 describes the noise levels in the x-, y- and z-axes received by the seismometer. It is expected that the noise level does not exceed the VBB and SP vertical and horizontal instrument noise level requirement. Even the highest noise peak, in 26.3 Hz, did not exceed the SP noise limit.

5 Discussion

Results presented in Figure 6 indicate that the mechanical noise has distinct comportments over the frequency spectrum. At low frequencies, from 10^{-4} Hz to 0.015

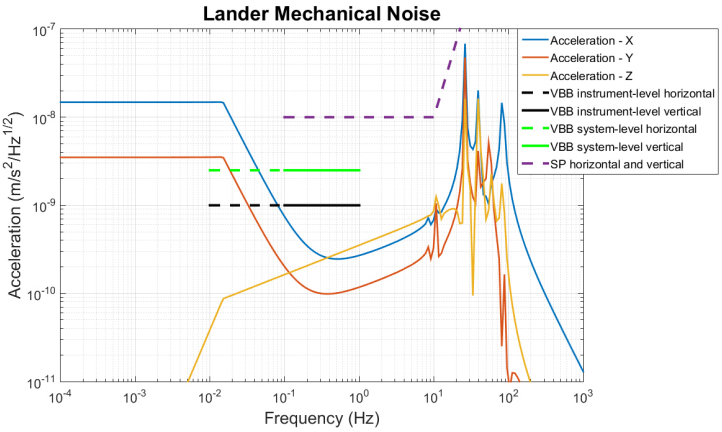

Figure 6: Lander mechanical noise.

Hz, it is possible to recognize a constant value for the horizontal components. As described in Section 4, the tilt noise of the horizontal components is dominant in low frequencies, increasing the values of the horizontal acceleration noise. The tilt noise effect is more evident when the horizontal components are compared with the vertical component, which registers noise from the direct motion of the footpad.

From 0.015 Hz to 3 Hz there is a linear decrease until 0.5 Hz followed by a linear increase described by the horizontal components and a constant linear increase for the vertical component. The decrease of the horizontal noise components is due to the fact that when the frequency increases, the tilt noise contribution decreases and the direct motion noise increases. Thus, at the minimum point of the curve there is an equality of these noises.

Finally, from 3 Hz to 100 Hz, the dynamic vibration modes from ground direct motion are visible in three components of noise. In this case, there are six natural frequencies of the lander: 8.40 Hz, 10.72 Hz, 26.13 Hz, 39.17 Hz, 54.16 Hz and 81.2 Hz, where the third mode has the maximum peak of $6.84{\cdot}10^{-8}$ $m^2s^{-2}Hz^{-1/2}$. However this maximum peak is within the SP noise limit.

Focusing on a better understanding of the mechanical noise response, parameters of the project were changed, in order to evaluate their contributions and impact on the frequency response, demonstrated in Figure 6. This analysis considered two points with the highest amplitudes: Point 1 is the acceleration at 0.015 Hz and Point 2 is the peak of the third mode of vibration. Table 4 presents the reference parameters that were being used in this paper.

Table 4: Reference parameters

Parameters	**Values**
Wind amplitude	125 $m^2s^{-2}Hz^{-1/2}$
Wind direction, x-y plane	45°
Ground stiffness R_s	6390 kN/m
Distance between SEIS and Lander	2.59 m
SEIS orientation with lander	180°

5.1 Variation of wind parameters

The first parameter evaluated was the wind amplitude. Figures 7 describes the variations of the mechanical noise amplitude at the Point 1 and Point 2. These responses indicated that the wind amplitude is related directly with the noise, which raised the tilt at the seismometer and led to a higher excitation of the vibrational modes. In both points there are an equally increase of the three noise components.

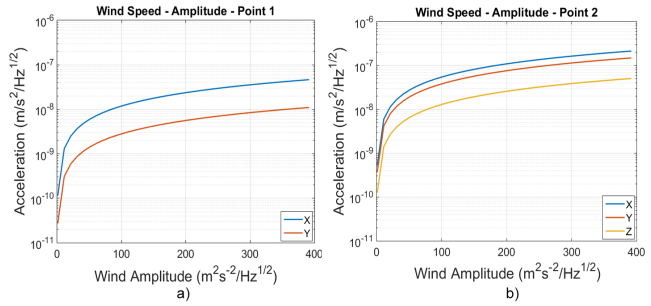

Figure 7: (a) Amplitude of mechanical noise in relation to wind amplitude at Point 1 and (b) Amplitude of mechanical noise in relation to wind amplitude at Point 2.

5.2 Variation of ground properties

After analysing effects of wind amplitude variations, the influence of ground proprieties was examined, specifically changing the values of the ground stiffness K_s.

Figure 8 indicates the mechanical noise at the Point 1 and Point 2. The stiffness increasing resulted in a decline of mechanical noise in both points, but with different orders of magnitude. At the Point 1 the decline was of 1000 $ms^{-2}Hz^{-1/2}$ and at the Point 2 of 10 $ms^{-2}Hz^{-1/2}$. A low stiffness means a soft soil, which is more susceptible to suffer deformations. Consequently, the high decrease of the noise level at the Point 1 was result of tilt increasing. On the other hand, a stiff soil facilitates propagation of direct motion. Even with a global reduction of noise, the disparity from Point 2 and Point 1 increases, explaining the dominance of direct ground motion noise.

Figure 9 exposes the variation of natural frequency from the third mode. This comportment of the natural frequency is explained by theory of vibrations [8], in which the resonant frequency is proportional to the square root of the stiffness. This property could be useful for the objective of the mission InSight, because it would be possible to determinate the soil stiffness of Mars verifying the position of the resonant frequencies.

5.3 Variation of distance between SEIS and lander center

The last parameter considered was the distance from the SEIS center to the lander center. Figure 11 presents

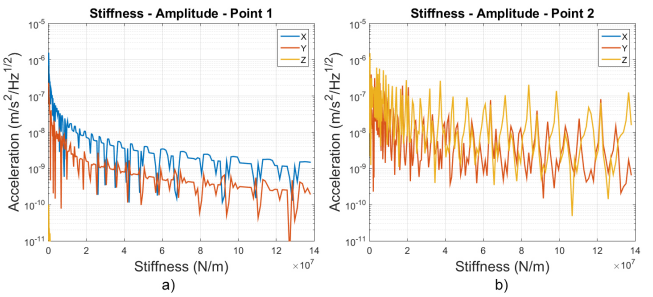

Figure 8: (a) Amplitude of mechanical noise in relation to stiffness at Point 1 and (b) Amplitude of mechanical noise in relation to stiffness at Point 2.

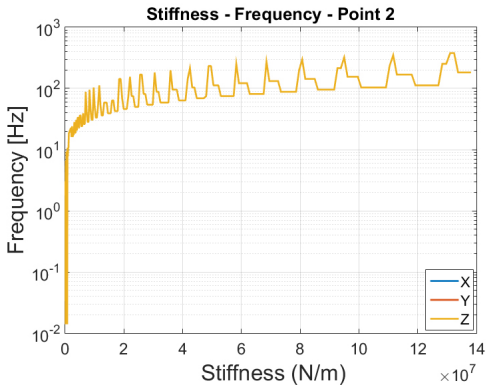

Figure 9: Variation of natural frequency of the third mode in relation to stiffness.

the evolution of mechanical noise at the Point 1 and at the Point 2. At both points, there are a maximum region of noise situated approximately 1 meter from SEIS to lander center. This is the closest position of SEIS center to the lander footpad, thus is advised to avoid this site when positioning the seismometer. From this place, all the mechanical noises decreased with the increasing of distances between the SEIS center and the lander footpads. There is an optimum distance of 4.60 meters in which tilt noise of y-acceleration axis is minimum. However, due to mechanical limitations, the lander cannot set down the seismometer at this distance.

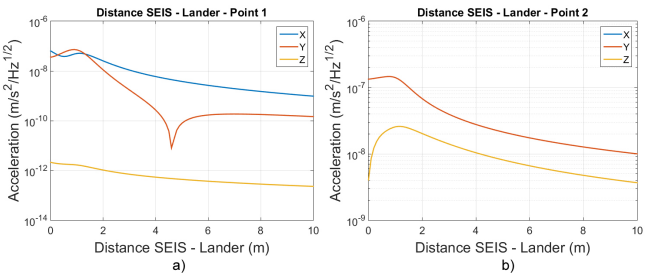

Figure 10: (a) Variation of mechanical noise in relation to SEIS and lander center at Point 1 and (b) Variation of mechanical noise in relation to SEIS and lander center at Point 2.

5.4 Model application in a real case

In terms of verifying our model, a real wind spectrum collected by the mission Viking Lander 1 was adopted. Figure 11 exposes a comparison between the employment of the real wind model and linear wind model.

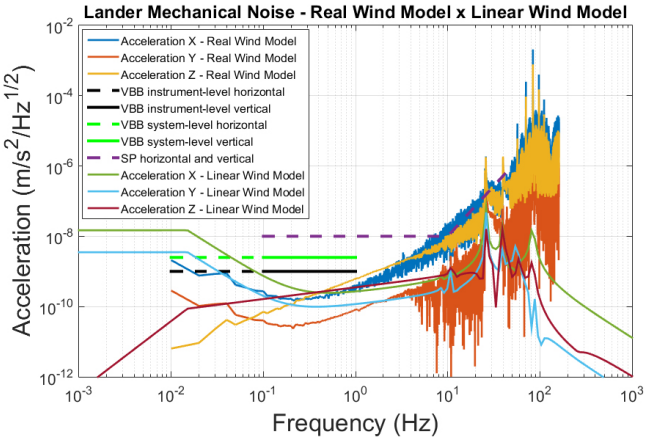

Figure 11: Real model and linear model comparison.

It is possible to observe that, at low frequencies, the noise components of the real wind model are smaller than that expected. At high frequencies, the noise is higher than that expected and it was above the SP noise limit. The linear wind model adopted the 1σ day time atmospheric conditions, though any changes in amplitude and direction of wind could affect the lander mechanical noise response.

Even considering all possible origins of errors, the linear wind model and the real wind model responses are similar. In both models, the changing of the tilt noise at low frequencies and the direct motion noise at high frequencies are visible. For high frequencies there are high amplitudes of acceleration due to an interpolation method used. The regions of the natural frequencies are almost the same, for example, the third mode of vibration of the real wind model is 0.20 Hz lower than the linear wind model.

6 Conclusions

Prior works analysed mechanical noises at low frequency. However, with the development of our project, it was possible to examine higher frequencies, employing a dynamic model. Previously just the very-broadband (VBB) sensor was analysed. Nonetheless, now the influence of noise in short-period (SP) sensor may also be considered.

Subsequently, to give continuity to this project, it would be beneficial make use of the filtering processes to minimize the mechanical noise. This could provide a more accurate detection of Martian soil seismic activity.

This paper studied an estimation of amplitude noise for a Martian day spectra correspondent to 70%, although other estimations could be analysed to verify the distinct noise responses.

Finally, we believe our project may be useful to improve the accuracy of the noise estimations and seismological prospecting on Mars, by means of project InSight and future missions.

References

[1] W. Bruce Banerdt and Sue Smrekar. Insight: Science and mission overview. 2012.

[2] P Lognonne, WB Banerdt, RC Weber, D Giardini, WT Pike, U Christensen, D Mimoun, J Clinton, V Dehant, R Garcia, et al. Science goals of seis, the insight seismometer package. In *Lunar and Planetary Science Conference*, volume 46, page 2272, 2015.

[3] Daniel Alazard and Christelle Cumer. *Satellite Dynamics Toolbox - Principle, User Guide and tutorials.*, 2014.

[4] Khalid HM Tantawi, Daniel Alazard, and Christelle Cumer. Linear dynamic modeling of spacecraft with various flexible appendages. In *World tantawi2008linear*, volume 17, pages 11148–11153, 2008.

[5] Mark D Ardema. *Newton-Euler Dynamics*. Springer Science & Business Media, 2006.

[6] Joseph Boussinesq. *Application des potentiels à l'étude de l'équilibre et du mouvement des solides élastiques: principalement au calcul des déformations et des pressions que produisent, dans ces solides, des efforts quelconques exercés sur une petite partie de leur surface ou de leur intérieur: mémoire suivi de notes étendues sur divers points de physique, mathematique et d'analyse*, volume 4. Gauthier-Villars, 1885.

[7] Taichi Kawamura Naomi Murdoch, David Mimoun and Philippe Lognonné. Evaluating the wind-induced mechanical noise on the insight seismometers. 2015.

[8] Frank Edwin Richart, John Russell Hall, and Richard D Woods. Vibrations of soils and foundations. 1970.

[9] Dhemaied Delage, Karakostas. The geotechnical properties of some martian regoliths simulants in link with the insight landing site. *Space Science Reviews*, 2016.

[10] Marcel Labarrère, Jean-Pierre Krief, Bernard Gimonet, Marc Pélegrin, and JP Krief. *Le filtrage et ses applications*. Cepadues, 1982.

[11] Timothy G Gutowski and Clive L Dym. Propagation of ground vibration: a review. *Journal of Sound and Vibration*, 49(2):179–193, 1976.